Novel synthesis of porous aluminium and its application in hydrogen storage

M. Veronica Sofianos [a,*], Drew A. Sheppard[a], Enrico Ianni[a], Terry D. Humphries[a], Matthew R. Rowles[a], Shaomin Liu[b], Craig E. Buckley[a]

[a]Department of Physics and Astronomy, Curtin University, GPO Box U1987, Perth, WA 6845, Australia.

[b]Department of Chemical Engineering, Curtin University, GPO Box U1987, Perth, WA 6845, Australia.

*Dr Maria Veronica Sofianos

Hydrogen Storage Research Group,

Fuels and Energy Technology Institute,

Department of Physics and Astronomy

Curtin University,

GPO Box U1987,

Perth, WA 6845,

Australia.

E-mail: mvsofianou@gmail.com

Fax: +61 8 9266 2377

Tel: +61 8 9266 7225

Abstract

A novel approach for confining $LiBH_4$ within a porous aluminium scaffold was applied in order to enhance its hydrogen storage properties, relative to conventional techniques for confining complex hydrides. The porous aluminium scaffold was fabricated by sintering $NaAlH_4$, which was in the form of a dense pellet, under dynamic vacuum. The final product was a porous aluminium scaffold with the Na and H_2 having been removed from the initial pellet. This technique contributed to achieving highly dispersed $LiBH_4$ particles that were also destabilised by the presence of the aluminium scaffold. In this study, the effectiveness of this novel fabrication method of confined/destabilised $LiBH_4$ was extensively investigated, which aimed to simultaneously improve the hydrogen release at lower temperature and the kinetics of the system. These properties were compared with the properties of other confined $LiBH_4$ samples found in the literature. As-synthesised samples were characterised using Scanning Electron Microscopy (SEM), X-ray Diffraction (XRD) and Nitrogen Adsorption measurements. The hydrogen storage capacity of all samples was analysed using temperature programmed desorption in order to provide a comprehensive survey of their hydrogen desorption properties. The porous aluminium scaffold has a wide pore size distribution with most of the porosity due to pores larger than 50 nm. Despite this the onset hydrogen desorption temperature (T_{des}) of the $LiBH_4$ infiltrated into the porous aluminiumscaffold was 200 °C lower than that of bulk $LiBH_4$ and 100 °C lower than that of nanosized $LiBH_4$. Partial cycling could be achieved below the melting point of $LiBH_4$ but the kinetics of hydrogen release decreased with cycle number.

Keywords: Hydrogen storage; Destabilisation; Nanocomposites; Aluminium scaffold; $LiBH_4$

1. Introduction

Over the last number of years, hydrogen has attracted a lot of attention in the scientific community as well as the automobile industry as an energy carrier for automobile applications [1, 2]. Utilising hydrogen as an energy store has multiple advantages, the most obvious being its low environmental impact, having near zero pollutant emissions when reversibly produced and converted to electricity in a fuel cell [3, 4]. Many challenges must be faced during the development of a hydrogen based economy, especially in the production of a suitable on-board hydrogen storage material, that will meet the hydrogen storage target (5.5 wt% H_2) set by the U.S. Department of Energy [5, 6].

A potential material for such application is lithium borohydride, $LiBH_4$, which is known from the literature to have a high theoretical hydrogen storage capacity of up to 18.5 wt% and a practical capacity up to 13.8 wt% [7]. $LiBH_4$ begins to desorb hydrogen according to eq. 1 at 370 °C, which continues up to a temperature of 600 °C depending on the conditions employed [8]. The decomposition product, LiH, is thermally stable and does not start desorbing hydrogen until 910 °C [9]. As such, reaching the theoretical hydrogen storage capacity of $LiBH_4$ is not feasible at temperatures lower than 600 °C and so only 13.8 wt% is practically achievable [10]. Not only does the high temperature of desorption inhibit practical use of this material, its reversible hydrogenation is problematic as temperatures of above 600 °C and 350 bar of hydrogen pressure are required [5, 11].

$$2LiBH_4 \rightarrow 2LiH + 2B + 3H_2 \tag{1}$$

There are two main strategies described in the literature for solving the challenges of reversible hydrogenation and also for decreasing the hydrogen desorption

temperature. One method is by thermodynamically destabilising $LiBH_4$ by the addition of a second phase such as a binary hydride, oxide, metal halide or a metal in order to reduce the enthalpy of dehydrogenation, with a resultant decrease of its decomposition temperature [4, 12-22]. This method is well known in the literature and has been applied to various metal hydrides with MgH_2 and $NaMgH_3$ showing particularly promising result [23]. To date, the most efficient destabilisation agent for $LiBH_4$ is Al, eq. 2, with a resulting theoretical hydrogen storage capacity of 8.3 wt% [10]. However, this system faces some drawbacks, such as poor kinetics of hydrogen reabsorption as well as product segregation and loss of hydrogen capacity upon cycling [13, 24].

$$2LiBH_4 + Al \leftrightarrow AlB_2 + 2LiH + 3H_2 \tag{2}$$

The second strategy applied in the literature is to improve the kinetics of metal hydrides by decreasing the particle size down to the nanoscale [25-34]. This can be achieved by confining the $LiBH_4$ into a mesoporous scaffold such as activated carbon, carbon aerogel, carbon black, carbon nanotubes/fibers, templated carbons, mesoporous silica and metal organic frameworks [8, 25, 26, 35-43]. The main disadvantage of using these materials as a scaffold is that they all contain oxygen. For instance, carbon aerogels and activated carbon typically contain between 4 wt% and 14 wt% of oxygen [44-46]. This is a significant drawback as most metal hydrides are strong reducing agents, and their oxidation within the scaffold leads to capacity loss upon cycling. Moreover, the hydrogen reabsorption reaction is exothermic which means that heat is produced during this procedure. These scaffolds are known to have poor thermal conductivity which causes the $LiBH_4$ to self-heat during the hydrogen absorption and hence hinders any further absorption[47]. Lastly, these porous scaffolds add an

additional weight penalty, even at high hydride loadings, making them unsuitable for storing hydrogen in vehicles.

Based on the literature so far, attempts have been made to combine confinement of a metal hydride together with a destabilising second phase [26, 48]. However, these efforts do not address the reactions between the oxygen in the scaffold and the metal hydrides, nor the poor thermal conductivity of the scaffolds employed. Mesoporous metal scaffolds (MMS) are a new type of materials that have been considered as an attractive solution for battery, fuel-cell and catalytic applications due to their robustness [49-51]. Only recently have such materials been synthesised as electrodes for battery applications[51]. According to our knowledge, no prior research has been conducted on the utilisation of MMS for the confinement and destabilisation of infiltrated metal or complex metal hydrides in the hydrogen storage community.

In this study, we report a novel approach for synthesising a porous aluminium scaffold using $NaAlH_4$ as a starting material. $LiBH_4$ has been melt infiltrated into this scaffold in order to obtain a $LiBH_4$/Al composite material as the final product. This novel metal scaffold serves as an oxygen-free porous substrate, which partially reacts with the confined complex metal hydride in a destabilising reaction. The remaining metal scaffold substantially improves the thermal conductivity of the hydride bed. The amount of the Al and the $LiBH_4$ encapsulated within it have been carefully calculated so that sufficient metal scaffold remains upon reaction with the complex metal hydride to maintain the structural integrity of the scaffold. Moreover, this confinement approach maintains the kinetic advantages of the confined metal hydride by limiting segregation of the desorption products.

2. Materials and methods

2.1 Sample preparation

All samples were prepared and handled in an argon (Ar) glovebox with oxygen (O_2) and moisture level (H_2O) less than 1 ppm in order to avoid sample contamination and to minimise any reactions with either O_2 or H_2O, as all chemicals used for the synthesis were air and moisture sensitive.

The $NaAlH_4$ (Sigma Aldrich ≥93%) used as a starting material for the fabrication of the porous aluminium scaffold was mixed with 2 mol.% $TiCl_3$ (Sigma Aldrich ≥99.999%) and ball milled under an Ar atmosphere at room temperature. The ball milling was performed using an Across International Planetary Ball Mill (PQ-N04) employing tempered steel vials. A rotational speed of 350 rpm was used, while a ball to powder ratio of 30:1 was achieved with an equal number of 10 mm and 6 mm diameter stainless steel balls. The total ball milling time was 4 hours excluding any pauses during the process. The rotation of the canisters was changed every 15 minutes with a 5 minute pause in between each rotation in order to minimise the increase of temperature inside the canisters.

After ball milling, the as prepared $NaAlH_4$ was pressed into a pellet using an 8 mm stainless steel die. The die was placed into a custom made vacuum bag in order to avoid any contamination of the pellet with O_2. The pellet was then sintered for 6 hours under dynamic vacuum at 450 °C using a Labec VTF 80/12 tube furnace with a ramping rate of 5 °C/min, before being left to slowly cool to room temperature.

$LiBH_4$ (Sigma Aldrich ≥90%) was melt infiltrated into the porous aluminium scaffold using a stainless steel reactor. To prevent $LiBH_4$ decomposition, the reactor was loaded with ~60 bar of H_2 pressure at room temperature and heated at 5 °C/min to

300°C where it was held isothermal for 30 minutes. The final pressure of H_2 in the reactor at 300 °C was ~70 bar H_2. The sample was then allowed to cool to room temperature. Four different weight percentages of $LiBH_4$ (10.5, 14.5, 21.4 and 27.4 wt%) were infiltrated into the aluminium scaffolds. All aluminium scaffolds used were sanded by hand, using P180 grit silicon carbide sandpaper prior to the infiltration process in order to remove the thin non-porous surface area (Fig.2 a,b) that was formed during the sintering procedure.

Table 1. Description of all synthesised samples, their total theoretical wt% of H that is contained in the pellet which is calculated from the equivalent wt% of $LiBH_4$ infiltrated in the pellets and the theoretical H_2 wt% according to eq. 2.

Description	Sample ID	Total Theoretical wt% of H contained in Pellet	Theoretical H_2 wt% of Pellet from eq. 2
Porous Al + 10.5 wt% $LiBH_4$	PAL-10	1.9	1.5
Porous Al + 14.5 wt% $LiBH_4$	PAL-14	2.8	2.1
Porous Al + 21.4 wt% $LiBH_4$	PAL-21	4.0	3.0
Porous Al + 27.4 wt% $LiBH_4$	PAL-27	5.1	3.8

2.2 Sample characterisation

The chemical analysis and phase observations of all samples were examined by powder X-ray diffraction (XRD) (Bruker D8 Advanced diffractometer) using CuK_α radiation. The measurements were performed using 0.3° for the divergence slit and 0.3° for the antiscattering slit. The measured 2θ range (20° - 80°) was scanned with a 0.03 step size, at 1.6 s/step and a rotational speed of 30 rpm. The accelerating voltage and applied current were 40 kV and 40 mA, respectively. XRD sample holders were

covered with a poly(methylmethacrylate) (PMMA) airtight bubble to prevent oxygen/moisture contamination during data collection. The PMMA airtight bubble results in a broad hump in XRD patterns centred at ~20° 2θ. Phase identification was accomplished using the International Centre for Diffraction Data Powder Diffraction File (PDF) cards. TOPAS Ver.5 was used to calculate a diffraction pattern that corresponds to a sample which has the same $LiBH_4$/Al ratio as PAL-27 [52, 53]. The X-ray diffraction patterns of the samples that are presented after their melt infiltration of $LiBH_4$ were in a pellet form, whereas the X-ray diffraction patterns of the samples after their Temperature Programmed Desorption experiments were crushed into a powder in order to obtain phase information from the entire sample and not only from their surface and upper layers close to their surface.

Morphological observations were carried out with a Neon 40EsB scanning electron microscope (SEM) from Zeiss (Zeiss, Germany). Specimens from the centre and surface of the pellets were prepared by fracturing the pellets and placing on small pieces of carbon tape before being coated with a 3 nm layer of platinum to produce a conductive layer in order to reduce charging of the sample during SEM. The exposure of the samples to air was minimised by using a custom made shuttle in which the specimens were transferred from the glovebox to the coating instrument and into the SEM chamber.

The porosity of the aluminium scaffold was analysed by nitrogen (N_2) adsorption/desorption experiments, which were conducted at 77 K using a Micromeritics ASAP 3020 system (Micromeritics, Nor-cross, GA, USA). The specific surface area of the scaffold was calculated from the N_2 adsorption data, at relative pressures between 0.05 and 0.30, by employing the Brunauer–Emmett–Teller (BET) multi-point method. The pore size distributions and volumes in the macro- and meso-

range were calculated using the Barrett–Joyner–Halenda (BJH) method from the desorption branch of the isotherm.
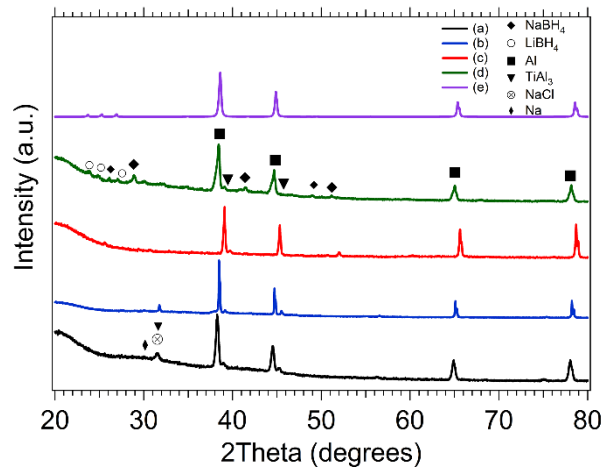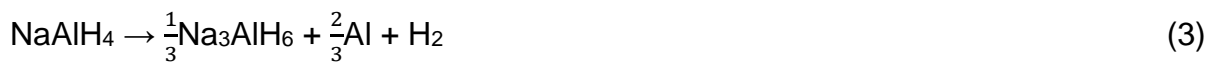
Temperature programmed desorption (TPD) measurements were undertaken on a computer controlled Sieverts/volumetric apparatus [20]. The sample temperature and pressure was recorded every 30 s using a K-type thermocouple with an accuracy of 0.1 °C at 419 °C and a digital pressure transducer (Rosemount 3051S) with a precision/accuracy of 14 mbar. H_2 desorption data was obtained in the temperature range, from room temperature to 250, 265 and 550 °C with a ramping rate of 5 °C/min. The temperature was kept isothermal at 250, 265 and 550 °C for 10 hours with final H_2 backpressures of between 0.8 and 1.4 bar generated during the desorption of the samples. For the sample that was previously desorbed at ~250 °C H_2 absorption was carried out in the pressure range of ~80 bar, and the sample was heated from room temperature to 250 °C for 10 h, with a ramping rate of 5 °C/min and finally cooled to room temperature.

3. Results and discussion

3.1 Characterisation of as prepared porous aluminium scaffold and infiltrated samples

The XRD patterns of the as prepared aluminium scaffold as well as that of the samples melt infiltrated with $LiBH_4$, are presented in Fig. 1(a-d). From the XRD pattern of the as prepared aluminium scaffold (Fig. 1(a)) it is obvious that the $NaAlH_4$ starting material used to synthesise the porous aluminium scaffold has completely decomposed into Al (JCPD 000011180) with only minor traces of Na (JCPD 000010832) remaining. It is well known from the literature that $NaAlH_4$ starts to decompose between 100 and 150 °C when $TiCl_3$ is added (eq. 3,4) [54, 55]. As the temperature was increased and reached 400 °C, NaH completely decomposed to Na

and H_2 (eq. 5) [55-59]. Na metal at that temperature, is in the molten state with 0.001 bar of vapour pressure [60, 61] and is therefore evaporated from the main mass of the pellet *via* dynamic vacuum (~0.0001 bar) applied during the sintering procedure and captured in a trap placed inside the reactor. The diffraction peaks that are observed at ~2θ = 32°, 39°, 46°, 55° and 75° are attributed to the $TiCl_3$ additive, which during the sintering procedure reacted with $NaAlH_4$ forming $TiAl_3$ (JCPD 040152440) and NaCl (JCPD 00010994) [54].

$$NaAlH_4 \rightarrow \frac{1}{3}Na_3AlH_6 + \frac{2}{3}Al + H_2 \qquad (3)$$

$$Na_3AlH_6 \rightarrow 3NaH + Al + \frac{3}{2}H_2 \qquad (4)$$

$$NaH \rightarrow Na + \frac{1}{2}H_2 \qquad (5)$$

Fig. 1. XRD patterns of (a) the as prepared porous aluminium scaffold, (b) PAL-10, (c) PAL-14, (d) PAL-27 melt infiltrated into the Al porous scaffold and (e) calculated diffraction pattern using TOPAS with the same quantities as PAL-27.

The penetration depth of the x-rays for the porous aluminium scaffold is 1 mm, which is 40 % of the height of the pellet. This indicates that only diffraction peaks from the surface and upper layers of the samples close to the surface are represented in Fig.

1. The XRD pattern of the infiltrated sample with the smallest loading, PAL-10, does not show diffraction peaks for $LiBH_4$ (Fig. 1b). This observation indicates that the $LiBH_4$ has entered the inner pores of the pellet *via* capillary action, leaving no traces on the surface or upper layers of the pellet or it is in an amorphous state. The PAL-14 (Fig. 1c) has a small diffraction peak that corresponds to $NaBH_4$ (JCPD 000381022), whereas the sample with the highest loading of the infiltrated metal hydride exhibits diffraction peaks of $LiBH_4$ (JCPD 040113748) and $NaBH_4$. Fig. 1e illustrates the calculated diffraction pattern of a powder sample having the same quantities of $LiBH_4$ and Al as the sample PAL-27. This pattern provides a better understanding of the intensities which correspond to $LiBH_4$ and Al for PAL-27 and whether the complex metal hydride has reached its maximum infiltrated amount which can occupy the majority of the pores. Moreover, the diffraction peak that corresponds to NaCl, which overlaps with the diffraction peak for $TiAl_3$, which is present for the as prepared aluminium scaffold as well as for the PAL-10 sample (Fig. 1a & b) disappears as the infiltrated amount of $LiBH_4$ increases in the next set of samples (Fig. 1c & d). The presence of $NaBH_4$ may be attributed to the fact that NaCl (eq. 6) or residual Na has reacted with $LiBH_4$ during the infiltration process in a metathesis reaction. Moreover, according to the literature, the structural phase transition of $LiBH_4$ with I, Cl, Na and K substitutions respectively has been studied and the results have shown that Na can substitute for Li when $LiBH_4$ reaches high temperatures [62]. Further investigation on this matter has to be conducted, by applying *in situ* X-ray diffraction experiments during the infiltration process.

$$NaCl + LiBH_4 \leftrightarrow NaBH_4 + LiCl \qquad (6)$$

The SEM micrographs of the surface, prior to sanding, and centre of the as prepared aluminium scaffold are presented in Fig. 2 a-d. It can be seen that a wide range of

pore sizes and voids are present in the scaffold. The larger voids present in the sample are most likely created during the compaction of the $NaAlH_4$ into a pellet that was used as a starting material for the synthesis of the aluminium scaffold (the $NaAlH_4$ pellet was 70% dense relative to the crystalline density of $NaAlH_4$). The mesopores and macropores may have formed during the sintering process of the pellet under dynamic vacuum. While the pellet was heated to 450 °C, H_2 and Na were removed from the mass of the pellet creating these pores. Once 450 °C had been reached, and this temperature sustained for 6 h, the Na present in the pellet vaporised and was partially extracted from the pellet.
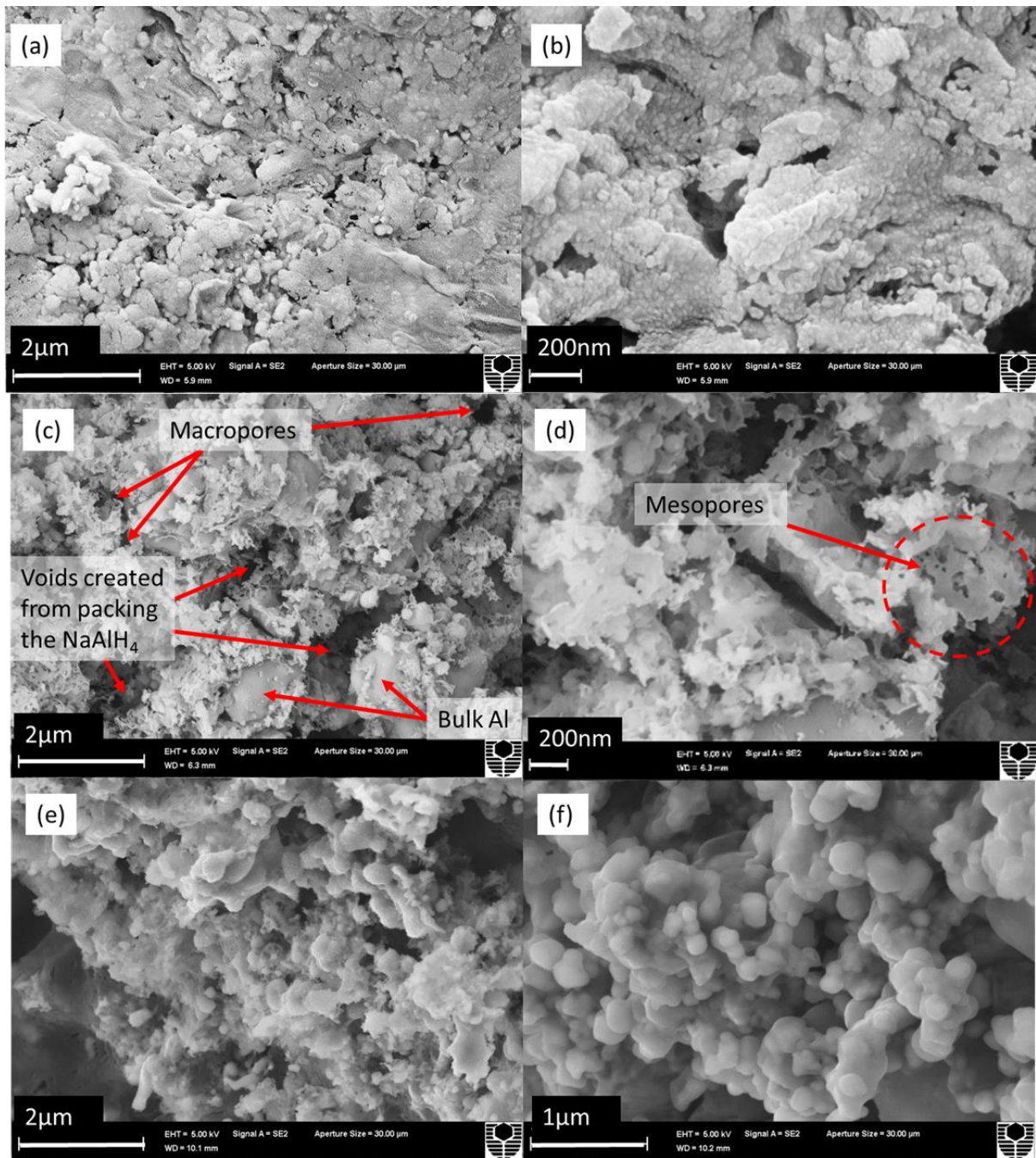
Fig. 2. SEM micrographs of the (a, b) surface prior to sanding (c,d) centre of the as prepared aluminium scaffold, and (e, f) centre of PAL-14 sample.

Fig. 2 (e, f) presents the SEM micrographs of a specimen cut from the interior part of the PAL-14 sample. It is noticeable from these micrographs that the majority of the pores are occupied by the complex metal hydride, which entered the inner pores of the scaffold *via* capillary condensation.

In Fig. 3 (a), the N_2 adsorption/desorption isotherms of the as prepared porous aluminium scaffold are presented. The isotherms are of a type II with associated H3 type hysteresis loop and a sharp capillary condensation step at high relative pressures (P/P_0 = 0.70-0.99) reflecting the large mesoporous and macroporous nature of the scaffold [63-65]. The lack of knee represents extremely weak adsorbate-adsorbent interaction indicating a lack of micropores [66]. The pore size distribution of the scaffold is presented in Fig. 3b and illustrates that the pores in the scaffold have polydispersity. A large number of pores with diameters ranging from 1.7 to 3.1 nm are present in the samples in comparison to the number of larger pores ranging between 20 - 40 nm in diameter. The total pore volume of the pellet is 1.51 cm^3/g, of which ~0.38 cm^3/g is due to the voids in the compacted starting material, which was calculated using the crystal density of $NaAlH_4$ as well as the physical (bulk) density of the pellet derived from its physical dimensions; 0.014 cm^3/g is due to the micropores and mesopores with diameter within the range of 1.7 - 40 nm as calculated from the BJH method (Table 2); and finally the remaining volume is due to the presence of macropores greater than 50 nm in size. These observations are in agreement with the SEM micrographs (Fig. 2). The BET surface area of the scaffold, 6.43 m^2/g is relatively small for a porous material and is due to the large volume of macropores. The relatively small surface area does not have a negative impact regarding the hydrogen desorption properties of the final material, as described in the thermal analysis section.
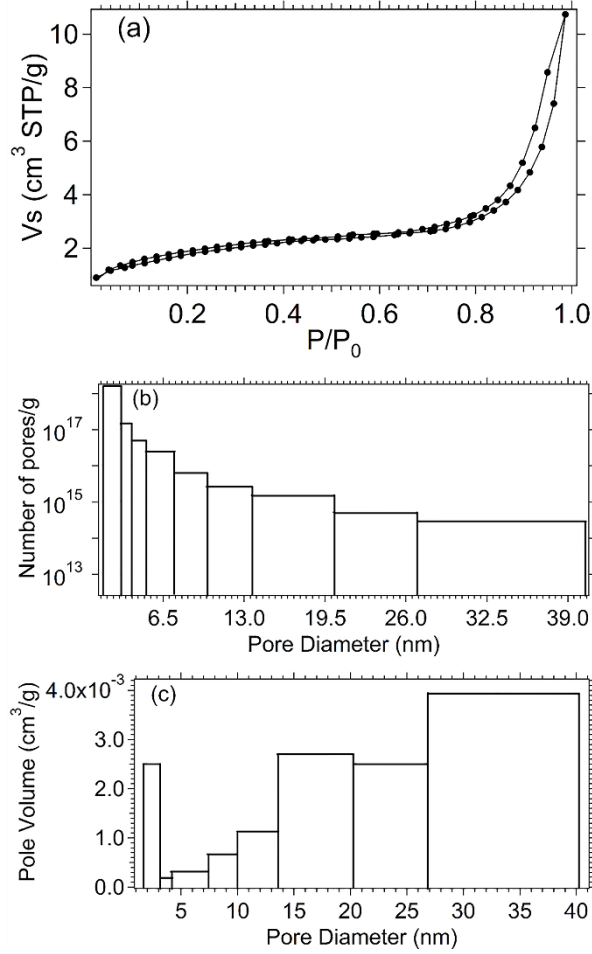
Fig. 3. (a) N₂ adsorption/desorption isotherm (b) pore size distribution diagram and (c) pore volume distribution diagram of the of the porous aluminium scaffold.

Table 2. Physical properties of porous aluminium scaffold.

Sample	Specific surface area (BET) (m^2/g)	Pore volume due to mesopores (cm^3/g)	Pore volume due to macropores (cm^3/g)	Pore volume due to voids (cm^3/g)	Total pore volume (cm^3/g)
Al porous scaffold	6.43	0.014	1.12	0.38	1.51

3.2 Thermal Analysis

The TPD curves of all samples are presented in Fig. 4. It is noticeable that the PAL-10 and PAL-27 samples start desorbing H_2 after the melting point of $LiBH_4$ ($T > 284$ °C). More specifically, the PAL-10 has reached its maximum H_2 desorption value (1.8 wt%) within 2 h, which includes the time required for the sample to reach the targeted temperature, 100 min. This experimental value does not match with the theoretical value (1.5 wt% H_2 for eq. 2 when considering the total mass of the pellet) calculated when the molar ratio of $LiBH_4$ to Al is 2:1. The reason for this, is that at temperatures above 500 °C, excess Al present from the porous scaffold is able to further react with the LiH formed from the first decomposition pathway (eq. 2), forming LiAl (eq. 7) [67].

$$2LiH + 2Al \rightarrow 2LiAl + H_2 \tag{7}$$

Moreover, the H_2 back pressure (0.82 bar) created for this sample during its thermal decomposition process, is below the equilibrium pressure that corresponds to eq. 7[67]. Hence, this reaction is thermodynamically favoured to take place[68]. As for the PAL-27, the maximum value of desorbed H_2 of 3.8 wt% was also reached within 2 h from the time the heating rate started. This value is equal to the theoretical H_2 capacity for 2:1 molar ratio of $LiBH_4$ to Al. In this case, the LiH formed was not further decomposed as the H_2 back pressure reached for this sample was higher than the equilibrium pressure of eq. 7. Thus, this reaction was not thermodynamically promoted. Also, the $LiBH_4$ which was infiltrated into the porous aluminium scaffold occupied the larger pores of the scaffold reducing its contact surface area. In contrast, the PAL-14 starts desorbing hydrogen below the melting point and, more significantly, the onset temperature of desorption is below 100 °C. The maximum H_2 desorbed wt% for this particular sample was 2.8. This is slightly higher than the theoretical calculated

value, and can be attributed to the uncertainties of the instrument used to conduct the TPD experiments.

The PAL-14 sample exhibited a different thermal behaviour in comparison to the rest of the samples. This fact may be attributed to the sample preparation procedure. More specifically, it has been shown from the XRD analysis of the samples (Fig. 1) that residual Na and NaCl from the sintering process of the porous aluminium pellet is mainly located on the surface. Therefore, prior to the infiltration procedure of the porous pellets, the surfaces were sanded by hand using P180 grit silicon carbide sandpaper in order to expose the pores of the scaffold by removing the thin non-porous layer formed during the sintering process (Fig. 2a,b) but also to reduce the presence of Na and NaCl. As this surface modification procedure is not automated, it may result in an inconsistent thickness removal from the surfaces between samples. This may then result in inconsistent loading of the $LiBH_4$ in the porous scaffolds even when the same infiltration conditions have been applied. The presence of Na as well as NaCl on the surface of the porous scaffold partially reacts with the molten $LiBH_4$ and hinders its entry into the inner pores of the scaffold by forming $NaBH_4$. Hence, the PAL-14 sample may exhibit the best thermal behaviour due to the smaller amount of $NaBH_4$ formed on its surface and therefore more molten $LiBH_4$ penetrated the inner pores of the scaffold in comparison to the rest of the samples and enhanced the hydrogen desorption properties. This possibility could be confirmed in future experiments by developing an automated or systematic method for surface removal.

TPD experiments were conducted at a heating rate of 5°C/min on sample PAL-21 up to temperatures below the melting point of $LiBH_4$, (250 and 264 °C) as seen in Fig. 5. The exact amount of $LiBH_4$ melt infiltrated in the scaffold is not repeatable. Thus, the wt% of $LiBH_4$ in that particular sample presented in Fig. 5 (PAL-21) is slightly different

to the one in Fig. 4 (PAL-14). Therefore, they are referred to with different sample names. On the 1st TPD measurement the sample releases 0.4 wt% H_2, equivalent to ~13.3% of the theoretical capacity, during the 50 minute heating time required to reach the set point temperature of 264°C. While the total quantity of H_2 released up to this temperature is low, the rate at which it is released suggests that $LiBH_4$ confined within sufficiently small pores results in a dramatic improvement in the kinetics of H_2 release. As far as the authors are aware, such dramatic improvements in kinetics below the melting point of $LiBH_4$ have not previously been reported in the literature when $LiBH_4$ has been destabilised with Al or confined into a porous scaffold as seen in Table 3. The volume of the mesopores in the Al framework (0.014 cm^3/g) could only accommodate ~3.4% of the total volume of $LiBH_4$ infiltrated into PAL-21 (0.214 g of $LiBH_4$: 0.786 g of Al = 0.409 cm^3 $LiBH_4$ per g of Al). This suggests that pores larger than 50 nm in diameter also contribute to improved H_2 release kinetics and detailed characterisation of pores in this size range, using mercury porosimetry for example, is required. Subsequent desorption cycles, performed after hydriding under a H_2 pressure of 80 bar for 10 h at 250-264°C, show both reduced kinetics and capacity, Fig. 5(b). However, it was found during the 3rd desorption cycle that raising the temperature by just 36°C to 300°C, above the melting point of $LiBH_4$, results in a dramatic increase in the H_2 release kinetics. This behaviour suggests that even below the melting point of $LiBH_4$ there are microstructural changes that occur during destabilisation with Al which results in slower kinetics for subsequent cycles.
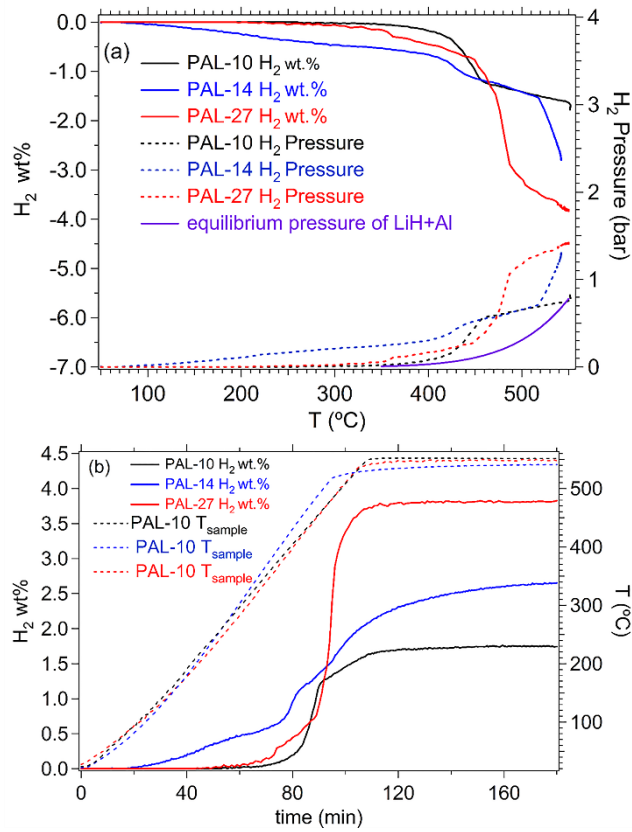
Fig. 4. Temperature programmed desorption results for PAL-10, PAL-14 and PAL-27 (a) wt% of hydrogen desorbed versus temperature and (b) versus time.
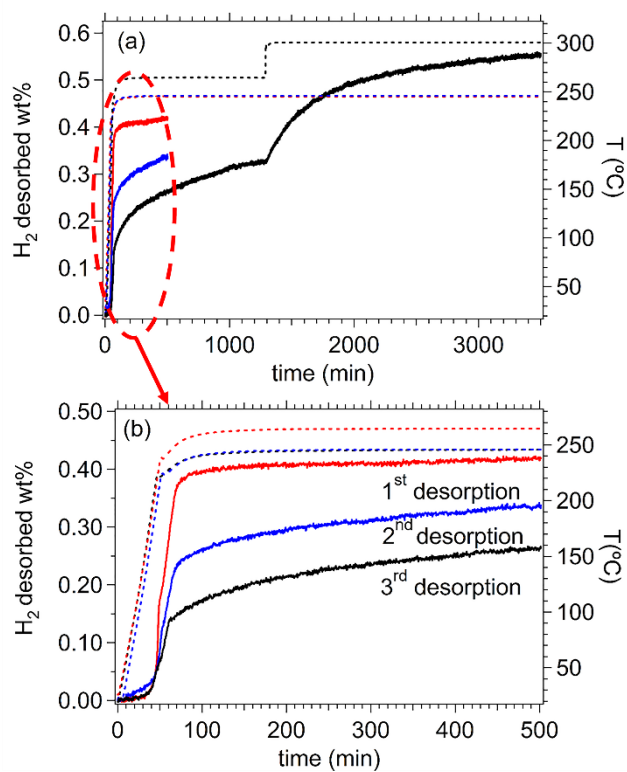
Fig. 5. Temperature programmed desorption of PAL-21 (a) after three desorption cycles below the melting point of LiBH$_4$. After the third cycle, the sample was heated just above the melting point (indicated by the upturn of 3rd desorption curve starting at ~1400 min) (b) magnification of the desorbing rates of the first three cycles.

Table 3. Thermal analysis results obtained from the literature of LiBH$_4$ destabilised from Al or nanoconfined.

Material	Method of Analysis	Conditions	Onset temperature of desorption (°C)	Maximum temperature of desorption (°C)	Reference
LiBH$_4$/Al	TPD-MS	Heating rate 5 °C/min under a constant flow of argon carrier	320	400	[10]
LiBH$_4$/Al	DSC	Heating rate 10°C/min under 1 bar of either argon or hydrogen with a flow rate of 100 mL/min	418	Not reported	[5]
LiBH$_4$/Al	TG-MS	Hydrogen backpressure of 0.001 bar	280	467	[67]
LiBH$_4$/Al	MS	Heating rate 10 °C/min under 1 bar Ar with a purging rate of 100 cm^3/min	310	480	[13]
LiBH$_4$ in graphite (HSAG-500)	TPD	Under an Ar flow (25 mL/min)	~200	~350	[69]
LiBH$_4$ in porous carbon with mainly 2-3 nm mesopores	TPD	Heating rate 5 °C/min under an Ar flow of 25 mL/min	284	400	[35]
LiBH$_4$ in aerogel scaffold with pore sizes in the range of 10-40 nm	TPD-MS	Heating rate 10 °C/min	284	445	[8]
LiBH$_4$ in aerogel scaffold with 13 nm pore size	TGA	Heating rates between 1 and 10 °C/min	230	381	[36]
LiBH$_4$ in activated carbon with 2 nm pore size	TGA	Heating rates between 1 and 10 °C/min	Not reported	375	[36]
LiBH$_4$ in aerogel with 25 nm pore size	TGA	Heating rates between 1 and 10 °C/min	Not reported	390	[36]
LiBH$_4$ in nanoporous graphite	TGA	Heating rates between 1 and 10 °C/min	Not reported	453	[36]

LiBH$_4$ in highly ordered porous carbon with 2 nm pore size	DSC	Heating rate 10 °C/min under 50 mL/min N$_2$ flow rate	Not reported	338	[37]
LiBH$_4$ in highly ordered porous carbon with 2 nm pore size	DSC	Heating rate 10 °C/min under a 50 mL/min N$_2$ flow rate	Not reported	342	[37]
LiBH$_4$ in carbon aerogels with 9 nm pore size	DSC	Heating rate 10 °C/min under 50 mL/min N$_2$ flow rate	Not reported	360	[37]
LiBH$_4$ carbon aerogels with 9 and 15 nm pore size	DCS	Heating rate 10 °C/min under 50 mL/min N$_2$ flow rate	Not reported	364	[37]
LiBH$_4$ physically mixed with highly ordered hexagonally packed cylindrical nanoporous carbon with a 2 nm average pore size	DSC	Heating rate 10 °C /min heating ramp under N$_2$ gas flow rate at 50 mL/min	284	339	[38]
LiBH$_4$ in highly ordered hexagonally packed cylindrical nanoporous carbon with a 2 nm average pore size	DSC	Heating rate 10 °C /min heating ramp under N$_2$ gas flow rate at 50 mL/min	250	330	[38]
LiBH$_4$ in amorphous SiO$_2$ scaffold with hexagonally ordered uniform mesopores with pore sizes from 5 to 9 nm	TPD	Heating rate of 5 °C/min under 25 mL/min Ar flow	150	280-300	[39]
LiBH$_4$ in Cu metal organic framework with a 0.9 nm pore size	TPD	Heating rate 2 °C /min	60	Not reported	[41]
LiBH$_4$ in activated carbon fibres with a 2.8 nm pore size	TPD	Heating rate of 5 °C /min under vacuum	246	Not reported	[34]

Table 4. Experimental (TPD) and theoretical quantity of desorbed H_2 from infiltrated LiBH$_4$. Theoretical values are for 2:1 molar ratio LiBH$_4$:Al (eq. 2) and total theoretical H capacity of the system.

Sample ID	Quantity of infiltrated LiBH$_4$ (wt%)	Onset temp. of H$_2$ desorpt. (°C)	Temp. of maxima H$_2$ release rate (°C)	Max P (bar)	Exp. H$_2$ capacity (wt%)	Total Theor. wt% of H in Pellet	Theor. H$_2$ wt% of Pellet from eq. 2
PAL-10	10.5	380	430	0.8	1.8	1.9	1.5
PAL-14	14.5	100	430, 530	1.3	2.8	2.8	2.1
PAL-27	27.4	350	460, 530	1.4	3.8	4.0	3.0

Fig. 6 illustrates the XRD diffraction patterns of all samples infiltrated with LiBH$_4$ after H_2 desorption measurements (eq. 2) performed up to 550°C. All samples were crushed into a powder after their thermal analysis in order to obtain a comprehensive diffraction pattern from the entire samples and not just from their surfaces. Diffraction peaks corresponding to AlB$_2$ (JCPD 040044983) are present in all samples, whereas LiH (JCPD 000090340) is present only in PAL-27 sample and are decomposition products of LiBH$_4$ destabilised by Al (eq. 2). Furthermore, diffraction peaks that correspond to LiAlO$_2$ (JCPD 040096438) are present due to oxidation of the scaffold during sample manipulation.
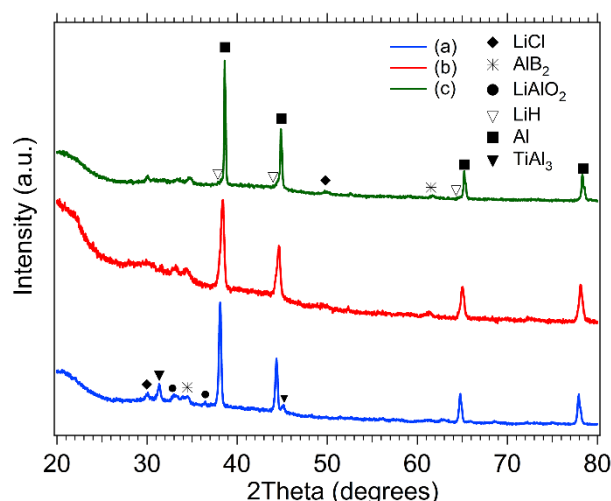
Fig. 6. XRD patterns of (a) PAL-10 (b) PAL-14 and (c) PAL-27 melt infiltrated into the aluminium scaffold after heating to 550 °C.

The XRD pattern of PAL-21 after its TPD measurement up to 264 °C is presented in Fig. 7. The decomposition products, AlB_2 and LiH, agree with those expected according to eq. 2. This corroborates the TPD experiments in that the onset desorption temperature of hydrogen is below the melting point of $LiBH_4$. Moreover, the presence of $NaBH_4$, which was formed during the infiltration process, explains the reduced H_2 capacity compared to the theoretical value (3.0 wt% H_2) if only $LiBH_4$ was present. $NaBH_4$ is known to decompose at higher temperatures, such as ~565 °C [70].

According to our obtained results from this study, further improvements have to be made in developing a consistent surface treatment of the pellets prior to melt infiltration of $LiBH_4$ in order to minimise the formation of $NaBH_4$ and to obtain reliably enhanced hydrogen desorption kinetics below the melting point of $LiBH_4$. The peaks that correspond to $TiAl_3$ and NaCl are associated with the $TiCl_3$ used as an additive for the starting material ($NaAlH_4$), whereas the reflections that correspond to Al are created by the porous metal scaffold.
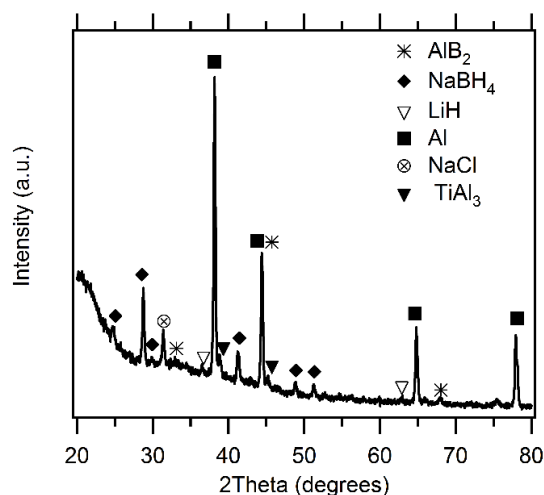
Fig. 7. XRD pattern of PAL-21 after the H$_2$ desorption experiments at 264 °C.

Porous metal scaffolds are a new category of materials with a wide range of applications covering many scientific fields, from biomedicine to environmental science. More specifically, they can be used in bone tissue engineering, Li ion batteries, hydrogen storage, gas sensing and finally in catalysis [71, 72]. Generally, the synthesis of metal porous scaffolds that do not contain noble metals is challenging, costly and scale up is difficult. The experimental conditions employed during the synthesis process have to be carefully controlled in order for the metal not to be oxidised and contaminate the final product. Moreover, most of the porous metal scaffolds that are presented in the literature to date are synthesised by using pure ionic liquids [51]. These methods either involve the electrodeposition of the targeted metal on a template or the selective dissolution of a less noble component of a metallic solid solution or alloy [73]. Ionic liquids are difficult to handle and are costly, thus scaling up the synthesis process for the mass production of these materials is not cost effective. This study presents a novel method for the synthesis of a porous aluminium scaffold by using NaAlH$_4$ as a starting material. Metal hydrides are cost effective, easy to handle (in comparison to ionic liquids) and can easily be used on a large scale in order to manufacture these novel scaffolds in large quantities. The most promising

aspect of this method is that it can be applied to the synthesis of various porous metal scaffolds with different metallic compositions or alloys provided a suitable hydride with a volatile element can be identified. This avoids facing any limitations that other electrochemical methods face, such as not achieving pure electrodeposited metals on the used templates. There are still challenges that have to be faced in order to improve this method. The sintering conditions of the metal hydrides need to be optimised since these conditions are the key factors controlling the purity and the porosity of the final product. The results obtained so far from this studied system are promising and are a stepping stone for the future optimisation of this final product from which many scientific fields can benefit from.

4. Conclusions

A porous aluminium scaffold in the form of a pellet was synthesised using $NaAlH_4$ as a starting material. The pores present in the scaffold are polydisperse according to the SEM micrographs and the N_2 adsorption/desorption analysis. These pores were created during the sintering process of the pellet due to the removal of hydrogen and sodium from the pellet whilst under dynamic vacuum. The XRD pattern after sintering reveals that the scaffold is mainly composed of Al. The XRD patterns after the infiltration of $LiBH_4$ into the scaffold at various quantities show that the complex metal hydride has entered the porous framework. Furthermore, the temperature programmed desorption measurements showed that all samples started desorbing hydrogen at temperatures much lower than the one that corresponds to bulk $LiBH_4$. The sample that was infiltrated with 14.49 wt% of the complex metal hydride started desorbing hydrogen at ~150 °C. Further improvements are required in order to increase the presence of mesopores in the scaffold, which in turn will enhance the confinement of $LiBH_4$ and reduce the hydrogen desorption temperature of this system,

to an even lower value than the one observed in this work. This will make it an ideal hydrogen storage system for use in automobile applications.

Acknowledgement

References

[1] L. Schlapbach, A. Züttel, Hydrogen-storage materials for mobile applications, Nature 414 (2001) 353-358.

[2] A. Züttel, A. Remhof, A. Borgschulte, O. Friedrichs, Hydrogen: the future energy carrier, Philos. Trans. A Math. Phys. Eng. Sci. 368 (2010) 3329-3342.

[3] K. Hirose, Materials towards carbon-free, emission-free and oil-free mobility: hydrogen fuel-cell vehicles--now and in the future, Philos. Trans. A Math. Phys. Eng. Sci. 368 (2010) 3365-3377.

[4] M.B. Ley, L.H. Jepsen, Y.-S. Lee, Y.W. Cho, J.M. Bellosta von Colbe, M. Dornheim, M. Rokni, J.O. Jensen, M. Sloth, Y. Filinchuk, J.E. Jørgensen, F. Besenbacher, T.R. Jensen, Complex hydrides for hydrogen storage – new perspectives, Mater. Today 17 (2014) 122-128.

[5] M. Meggouh, D.M. Grant, G.S. Walker, Optimizing the destabilization of $LiBH_4$ for hydrogen storage and the effect of different Al sources, J. Phys. Chem. C 115 (2011) 22054-22061.

[6] Energy.Gov, Office of Energy Efficiency & Renewable Energy, http://energy.gov/eere/fuelcells/hydrogen-storage, 2016 (13.07.2016 accessed).

[7] A. Züttel, P. Wenger, S. Rentsch, P. Sudan, P. Mauron, C. Emmenegger, $LiBH_4$ a new hydrogen storage material, J. Power Sources 118 (2003) 1-7.

[8] S. Cahen, J.B. Eymery, R. Janot, J.M. Tarascon, Improvement of the $LiBH_4$ hydrogen desorption by inclusion into mesoporous carbons, J. Power Sources 189 (2009) 902-908.

[9] J.J. Vajo, F. Mertens, C.C. Ahn, R.C. Bowman, B. Fultz, Altering hydrogen storage properties by hydride destabilization through alloy formation: LiH and MgH_2 destabilized with Si, J. Phys. Chem. B 108 (2004) 13977-13983.

[10] J. Yang, A. Sudik, C. Wolverton, Destabilizing $LiBH_4$ with a Metal (M = Mg, Al, Ti, V, Cr, or Sc) or Metal Hydride (MH_2 = MgH_2, TiH_2, or CaH_2), J. Phys. Chem. C 111 (2007) 19134-19140.

[11] S.-A. Jin, J.-H. Shim, Y.W. Cho, K.-W. Yi, O. Zabara, M. Fichtner, Reversible hydrogen storage in $LiBH_4$–Al–LiH composite powder, Scr. Mater. 58 (2008) 963-965.

[12] P. Sridechprasat, A. Siangsai, B. Kitiyanan, S. Kulprathipanja, P. Rangsunvigit, Effects of initial pressure on the decomposition of $LiBH_4$ and MgH_2 mixture, Clean Technol. Envir. 17 (2015) 1239-1246.

[13] X. Yu, G. Xia, Z. Guo, H. Liu, Dehydrogenation/rehydrogenation mechanism in aluminum destabilized lithium borohydride, J. Mater. Res. 24 (2011) 2720-2727.

[14] D. Liu, Q. Liu, T. Si, Q. Zhang, F. Fang, D. Sun, L. Ouyang, M. Zhu, Superior hydrogen storage properties of $LiBH_4$ catalyzed by $Mg(AlH_4)_2$, Chem. Comm. 47 (2011) 5741-5743.

[15] M. Au, A.R. Jurgensen, W.A. Spencer, D.L. Anton, F.E. Pinkerton, S.-J. Hwang, C. Kim, R.C. Bowman, Stability and reversibility of lithium borohydrides doped by metal halides and hydrides, J. Phys. Chem. C 112 (2008) 18661-18671.

[16] J.J. Vajo, W. Li, P. Liu, Thermodynamic and kinetic destabilization in $LiBH_4$/Mg_2NiH_4: promise for borohydride-based hydrogen storage, Chem. Comm. 46 (2010) 6687-6689.

[17] H.-W. Li, Y. Yan, S.-i. Orimo, A. Züttel, C.M. Jensen, Recent progress in metal borohydrides for hydrogen storage, Energies 4 (2011) 185-214.

[18] Y. Zhou, Y. Liu, W. Wu, Y. Zhang, M. Gao, H. Pan, Improved hydrogen storage properties of $LiBH_4$ destabilized by in situ formation of MgH_2 and LaH_3, J. Phys. Chem. C 116 (2012) 1588-1595.

[19] Y. Zhou, Y. Liu, Y. Zhang, M. Gao, H. Pan, Functions of MgH_2 in hydrogen storage reactions of the 6$LiBH_4$-CaH_2 reactive hydride composite, Dalton Trans. 41 (2012) 10980-10987.

[20] K. Wang, X. Kang, J. Ren, P. Wang, Nanostructured graphite-induced destabilization of $LiBH_4$ for reversible hydrogen storage, J. Alloys Compd. 685 (2016) 242-247.

[21] J. Zhang, P. Li, Q. Wan, F. Zhai, A.A. Volinsky, X. Qu, Superior destabilization effects of $LiBH_4$ with the addition of nano-sized nickel ferrite $NiFe_2O_4$, RSC Adv. 5 (2015) 81212-81219.

[22] G. Tu, X. Xiao, T. Qin, Y. Jiang, S. Li, H. Ge, L. Chen, Significantly improved de/rehydrogenation properties of lithium borohydride modified with hexagonal boron nitride, RSC Adv. 5 (2015) 51110-51115.

[23] A.-L. Chaudhary, M. Paskevicius, D.A. Sheppard, C.E. Buckley, Thermodynamic destabilisation of MgH_2 and $NaMgH_3$ using Group IV elements Si, Ge or Sn, J. Alloys Compd. 623 (2015) 109-116.

[24] J.W. Kim, O. Friedrichs, J.-P. Ahn, D.H. Kim, S.C. Kim, A. Remhof, H.-S. Chung, J. Lee, J.-H. Shim, Y.W. Cho, A. Züttel, K.H. Oh, Microstructural change of $2LiBH_4$/Al with hydrogen sorption cycling: Separation of Al and B, Scr. Mater. 60 (2009) 1089-1092.

[25] P. Adelhelm, P.E. de Jongh, The impact of carbon materials on the hydrogen storage properties of light metal hydrides, J. Mater. Chemi. 21 (2011) 2417-2427.

[26] P. Javadian, D.A. Sheppard, C.E. Buckley, T.R. Jensen, Hydrogen storage properties of nanoconfined $LiBH_4$–$Ca(BH_4)_2$, Nano Energy 11 (2015) 96-103.

[27] M. Paskevicius, D.A. Sheppard, C.E. Buckley, Thermodynamic changes in mechanochemically synthesized magnesium hydride nanoparticles, J. Am. Chem. Soc. 132 (2010) 5077-5083.

[28] M. Paskevicius, H.-Y. Tian, D.A. Sheppard, C.J. Webb, M.P. Pitt, E.M. Gray, N.M. Kirby, C.E. Buckley, Magnesium hydride formation within carbon aerogel, J. Phys. Chem. C 115 (2011) 1757-1766.

[29] S. Chumphongphan, U. Filsø, M. Paskevicius, D.A. Sheppard, T.R. Jensen, C.E. Buckley, Nanoconfinement degradation in $NaAlH_4$/CMK-1, Int. J. Hydrogen Energy 39 (2014) 11103-11109.

[30] E. Callini, P.Á. Szilágyi, M. Paskevicius, N.P. Stadie, J. Réhault, C.E. Buckley, A. Borgschulte, A. Züttel, Stabilization of volatile Ti(BH$_4$)3by nano-confinement in a metal–organic framework, Chem. Sci. 7 (2016) 666-672.

[31] H.Y. Tian, C.E. Buckley, M. Paskevicius, D.A. Sheppard, Hydrogen storage in carbon aerogels, Pan Stanford Publishing, Singapore, 2012.

[32] A. Surrey, C. Bonatto Minella, N. Fechler, M. Antonietti, H.-J. Grafe, L. Schultz, B. Rellinghaus, Improved hydrogen storage properties of LiBH$_4$ via nanoconfinement in micro- and mesoporous aerogel-like carbon, Int. J. Hydrogen Energy 41 (2016) 5540-5548.

[33] J. Shao, X. Xiao, X. Fan, X. Huang, B. Zhai, S. Li, H. Ge, Q. Wang, L. Chen, Enhanced hydrogen storage capacity and reversibility of LiBH4 nanoconfined in the densified zeolite-templated carbon with high mechanical stability, Nano Energy 15 (2015) 244-255.

[34] S. Thiangviriya, R. Utke, LiBH$_4$ nanoconfined in activated carbon nanofiber for reversible hydrogen storage, Int. J. Hydrogen Energy 40 (2015) 4167-4174.

[35] J. Gao, P. Ngene, I. Lindemann, O. Gutfleisch, K.P. de Jong, P.E. de Jongh, Enhanced reversibility of H$_2$ sorption in nanoconfined complex metal hydrides by alkali metal addition, J. Mater. Chem. 22 (2012) 13209.

[36] A.F. Gross, J.J. Vajo, S.L. Van Atta, G.L. Olson, Enhanced Hydrogen Storage Kinetics of LiBH$_4$ in Nanoporous Carbon Scaffolds, J. Phys. Chem. C 112 (2008) 5651-5657.

[37] X. Liu, D. Peaslee, C.Z. Jost, T.F. Baumann, E.H. Majzoub, Systematic Pore-Size Effects of Nanoconfinement of LiBH$_4$: Elimination of Diborane Release and Tunable Behavior for Hydrogen Storage Applications, Chem. Mater. 23 (2011) 1331-1336.

[38] X. Liu, D. Peaslee, C.Z. Jost, E.H. Majzoub, Controlling the Decomposition Pathway of LiBH4 via Confinement in Highly Ordered Nanoporous Carbon, J. Phys. Chem. C 114 (2010) 14036-14041.

[39] P. Ngene, P. Adelhelm, A.M. Beale, K.P. de Jong, P.E. de Jongh, LiBH4/SBA-15 Nanocomposites Prepared by Melt Infiltration under Hydrogen Pressure: Synthesis and Hydrogen Sorption Properties, J. Phys. Chem. C 114 (2010) 6163-6168.

[40] T.K. Nielsen, F. Besenbacher, T.R. Jensen, Nanoconfined hydrides for energy storage, Nanoscale 3 (2011) 2086-2098.

[41] W. Sun, S. Li, J. Mao, Z. Guo, H. Liu, S. Dou, X. Yu, Nanoconfinement of lithium borohydride in Cu-MOFs towards low temperature dehydrogenation, Dalton Trans. 40 (2011) 5673-5676.

[42] H.Y. Tian, C.E. Buckley, S. Mule, M. Paskevicius, B.B. Dhal, Preparation, microstructure and hydrogen sorption properties of nanoporous carbon aerogels under ambient drying, Nanotechnology 19 (2008) 475605.

[43] H.Y. Tian, C.E. Buckley, D.A. Sheppard, M. Paskevicius, N. Hanna, A synthesis method for cobalt doped carbon aerogels with high surface area and their hydrogen storage properties, Int. J. Hydrogen Energy 35 (2010) 13242-13246.

[44] S.A. Al-Muhtaseb, J.A. Ritter, Preparation and Properties of Resorcinol-Formaldehyde Organic and Carbon Gels, Adv. Mater. 15 (2003) 101-114.

[45] H.P. Boehm, Some aspects of the surface chemistry of carbon blacks and other carbons, Carbon 32 (1994) 759-769.

[46] R. Fu, B. Zheng, J. Liu, S. Weiss, J.Y. Ying, M.S. Dresselhaus, G. Dresselhaus, J. Satcher, T. Baumann, Studies of the chemical and pore structures of the carbon aerogels synthesized by gelation and supercritical drying in isopropanol, J. Appl. Polym. Sci. 91 (2004) 3060-3067.

[47] X. Lu, O. Nilsson, J. Fricke, R.W. Pekala, Thermal and electrical conductivity of monolithic carbon aerogels, J. Appl. Phys. 73 (1993) 581-584.

[48] A. Ampoumogli, G. Charalambopoulou, P. Javadian, B. Richter, T.R. Jensen, T. Steriotis, Hydrogen desorption and cycling properties of composites based on mesoporous carbons and a $LiBH_4$–$Ca(BH_4)_2$ eutectic mixture, J. Alloys Compd. 645 (2015) 480-484.

[49] Y. Bi, Y. Zheng, Y. Li, Microstructure and mechanical properties of sintered porous magnesium using polymethyl methacrylate as the space holder, Mater. Lett. 161 (2015) 583-586.

[50] J.J. de Damborenea, M.A. Larosa, M.A. Arenas, J.M. Hernández-López, A.L. Jardini, M.C.F. Ierardi, C.A.C. Zavaglia, R.M. Filho, A. Conde, Functionalization of Ti_6Al_4V scaffolds produced by direct metal laser for biomedical applications, Mater. Des. 83 (2015) 6-13.

[51] L.H.S. Gasparotto, A. Prowald, N. Borisenko, S.Z. El Abedin, A. Garsuch, F. Endres, Electrochemical synthesis of macroporous aluminium films and their behavior towards lithium deposition/stripping, J. Power Sources 196 (2011) 2879-2883.

[52] Y. Filinchuk, D. Chernyshov, R. Cerny, Lightest Borohydride Probed by Synchrotron X-ray Diffraction: Experiment Calls for a New Theoretical Revision, J. Phys. Chem. C 112 (2008) 10579-10584.

[53] R.W. G Wyckoff, Crystal structures 1, second edition, Interscience Publisher, New York (1963).

[54] T. Dobbins, M. Abrecht, Y. Uprety, K. Moore, An x-ray photoemission electron microscopy study of the formation of Ti-Al phases in 4 mol% $TiCl_3$ catalyzed $NaAlH_4$ during high energy ball milling, Nanotechnology 20 (2009) 2040141-2040149.

[55] C.P. Balde, H.A. Stil, A.M.J. vanderEerden, K.P. deJong, J.H. Bitter, Active Ti Species in TiCl$_3$-Doped NaAlH$_4$. Mechanism for Catalyst Deactivation, J. Phys. Chem. C 111 (2007) 2797-2802.

[56] M. Felderhoff, K. Klementiev, W. Grünert, B. Spliethoff, B. Tesche, J.M. Bellosta von Colbe, B. Bogdanovi, M. Hrtel, A. Pommerin, F. Schüth, C. Weidenthaler, Combined TEM-EDX and XAFS studies of Ti-doped sodium alanate, Phys. Chem. Chem. Phys. 6 (2004) 4369-4374.

[57] A.G. Haiduc, H.A. Stil, M.A. Schwarz, P. Paulus, J.J.C. Geerlings, On the fate of the Ti catalyst during hydrogen cycling of sodium alanate, J. Alloys Compd. 393 (2005) 252-263.

[58] T.D. Humphries, D. Birkmire, B.C. Hauback, G.S. McGrady, C.M. Jensen, In situ high pressure NMR study of the direct synthesis of NaAlH4, Phys. Chem. Chem. Phys. 15 (2013) 6179-6181.

[59] T.D. Humphries, J.W. Makepeace, S. Hino, W.I.F. David, B.C. Hauback, Regeneration of sodium alanate studied by powder in situ neutron and synchrotron X-ray diffraction, J. Mater. Chem. A 2 (2014) 16594-16600.

[60] D.M. Banus, J.J. McSharry, E.A. Sullivan, Sodium-sodium hydride-hydrogen system at 500-600°, J. Am. Chem. Soc. 77 (1955) 2007-2010.

[61] W. Klostermeier, E.U. Franck, Liquid Mixtures of Sodium and Sodium Hydride at High Pressures and Temperatures, Ber. Bunsen-Ges. Phys. Chem., 86 (1982) 606-612.

[62] N. Bernstein, M.D. Johannes, K. Hoang, First-principles free energy calculations of the structural phase transition in LiBH$_4$with I, Cl, Na, and K substitution, Phys. Rev. B 88 (2013) 2201021-2201025.

[63] F. Su, X.S. Zhao, Y. Wang, J. Zeng, Z. Zhou, J.Y. Lee, Synthesis of graphitic ordered macroporous carbon with a three-dimensional interconnected pore structure for electrochemical applications, J. Phys. Chem. B 109 (2005) 20200-20206.

[64] L. Yan, X. Bo, Y. Zhang, L. Guo, Facile green synthesis of nitrogen-doped porous carbon and its use for electrocatalysis towards nitrobenzene and hydrazine, Electrochim. Acta 137 (2014) 693-699.

[65] C. Zhao, W. Wang, Z. Yu, H. Zhang, A. Wang, Y. Yang, Nano-CaCO3as template for preparation of disordered large mesoporous carbon with hierarchical porosities, J. Mater. Chem. 20 (2010) 976-980.

[66] K.S.W. Sing, Reporting physisorption data for gas/solid systems with special reference to the determination of surface area and porosity (Recommendations 1984), Pure Appl. Chem. 57 (1985) 603-619.

[67] Y. Zhang, Q. Tian, J. Zhang, S.-S. Liu, L.-X. Sun, The Dehydrogenation Reactions and Kinetics of $2LiBH_4-Al$ Composite, J. Phys. Chem. C, 113 (2009) 18424-18430.

[68] E. Veleckis, Thermodynamic investigation of the Li·Al and Li·Pb systems by the hydrogen titration method, J Less Common Met 73 (1980) 49-60.

[69] J. Gao, P. Ngene, M. Herrich, W. Xia, O. Gutfleisch, M. Muhler, K.P. de Jong, P.E. de Jongh, Interface effects in $NaAlH_4$–carbon nanocomposites for hydrogen storage, Int. J. Hydrogen Energy 39 (2014) 10175-10183.

[70] P. Martelli, R. Caputo, A. Remhof, P. Mauron, A. Borgschulte, A. Züttel, Stability and Decomposition of $NaBH_4$, J. Phys. Chem. C 114 (2010) 7173-7177.

[71] K.M. Kulinowski, P. Jiang, H. Vaswani, V.L. Colvin, Porous metals from colloidal templates, Adv. Mater 12 (2000) 833-838.

[72] G. Ryan, A. Pandit, D.P. Apatsidis, Fabrication methods of porous metals for use in orthopaedic applications, Biomaterials 27 (2006) 2651-2670.

[73] O.M. Suarez, E.G. Estremera, R. Soler, A. Declet, A.J. Hernandez-Maldonado, Fabrication of porous and nanoporous aluminum via selective dissolution of Al-Zn alloys, Adv. Mater. Sci. Eng. 2014 (2014) 1-6.